Supplementary Information for

Disentangling surface atomic motions from surface field effects in ultrafast low-energy electron diffraction

Chiwon Lee, Alexander Marx, Günther H. Kassier, R.J. Dwayne Miller†

This file includes:

Supplementary Notes

Note 1: Data collection and image processing

For both, the direct and diffracted beam measurements, and for each Δt, we acquired a static image (probe only), an excitation laser background image (pump only), and a pump-probe image, in a sequential way. The camera readout time is approximately 1.1 sec between each acquisition. After the course of the image acquisition at a certain Δt, the delay line was changed by the interval of 3.3 ps, and the measurement was repeated in the observable time window range from Δt = -233 ps to 400.3 ps for the direct beam case and from Δt = -133 ps to 433.3 ps for the diffracted beam case. Difference maps were obtained by subtraction of the probe-only and the pump-only images from the pump-probe images, and addition of the camera background image recorded prior to the Δt scan (to compensate for double cancelling of the detector noise). Integrated intensities were obtained by defining regions-of-interest (ROIs) around the image centre (direct beam experiments) or the Bragg reflections (diffraction experiments) and summing up the values of all pixels within the ROIs. The ROI size for the direct beam experiment was 30 pixels by 30 pixels (≅ 1.7 mm by 1.7 mm as indicated in the red box in Fig. 1B), and that for the diffracted beam experiment was 10 pixels by 10 pixels, covering a single Bragg spot. The estimated electron detector resolution was approximately 50 µm. Six-fold symmetry of the diffraction pattern was assumed and used to increase the S/N by averaging over symmetry-equivalent Bragg spots. Absolute differences, ΔI, obtained by integration of the difference map were converted to relative intensities $\Delta I/I_{\mathrm{ref}}$ by using values obtained by integration of the probe only images as reference intensities.

Note 2: Data analysis

For a given region-of-interest (ROI) let $I(\Delta t)$ be the background-corrected and integrated intensity at time Δt after laser excitation (nominal delay). Let $I_{\mathrm{ref}}(\Delta t)$ denote the intensity at the ROI if no effect is present, neither the surface field effect nor the excess Debye-Waller effect due to temperature changes of the sample following photo-excitation. Thus, $I_{\mathrm{ref}}(\Delta t) = I(\Delta t)$ for $\Delta t < 0$. We also assume that each effect changes the observed intensity separately by independent factors x_{SF} and x_{DW}. Then, the combined effect is given by the product:

$$\frac{I(\Delta t)}{I_{\mathrm{ref}}(\Delta t)} = x_{\mathrm{SF}}(\Delta t)x_{\mathrm{DW}}(\Delta t) \qquad (1)$$

where, I/I_{ref} is the relative intensity, which can be expressed by the relative intensity changes, $\Delta I/I_{\mathrm{ref}}$, via the following relation:

$$\frac{\Delta I}{I_{\mathrm{ref}}} = \frac{I(\Delta t) - I_{\mathrm{ref}}(\Delta t)}{I_{\mathrm{ref}}(\Delta t)} = \frac{I}{I_{\mathrm{ref}}} - 1 \qquad (2)$$

In the case that only a single effect is active, one of the factors would be identical to 1.

In the following, the time argument is replaced by the true delay $t = \Delta t - t_0$ which is the nominal delay Δt corrected for an unknown offset t_0 (to be fitted) between the arrival of the probe and the pump pulse at the sample (arrival times measured at pulse maximum).

Note 3: Debye-Waller effect.

According to the Debye-Waller theory, the intensity of a Bragg reflection, $I_{(\mathrm{hk})}(T_\mathrm{l})$, (hk) Miller indices, is affected by the lattice temperature, T_l, of the diffracting crystal (two-dimensional case) as:

$$I_{(\mathrm{hk})}(T_\mathrm{l}) = I_{(\mathrm{hk}),0} \cdot exp\left\{-\frac{1}{2} < u(T_\mathrm{l})^2 > G_{(\mathrm{hk})}^2\right\} \quad (3)$$

where $I_{(\mathrm{hk}),0}$, $< u(T_\mathrm{l})^2 >$, and $G_{(\mathrm{hk})}$ are the scattered intensity of the rigid lattice (at zero Kelvin), the in-plane mean square atomic displacement dependent on T_l, and the reciprocal lattice vector of the (hk) lattice points, respectively. Assuming that $< u(T_\mathrm{l})^2 >$ of carbon atoms in graphene is proportional to T_l, we reformulate Supplementary Equation (3) with respect to $T_\mathrm{l}(t)$ for the respective spot orders:

$$\frac{I_{(10)}(T_\mathrm{l}(t))}{I_{(10),\mathrm{ref}}} = exp\{-p(T_\mathrm{l}(t) - T_{\mathrm{l,ref}})G_{(10)}^2\} \quad (4)$$

$$\frac{I_{(11)}(T_\mathrm{l}(t))}{I_{(11),\mathrm{ref}}} = exp\{-p(T_\mathrm{l}(t) - T_{\mathrm{l,ref}})G_{(11)}^2\} = exp\{-p(T_\mathrm{l}(t) - T_{\mathrm{l,ref}})G_{(10)}^2(G_{(11)}/\mathrm{G}_{(10)})^2\} \quad (5)$$

where, p is a constant. $T_{\mathrm{l,ref}}$ is the lattice temperature before excitation, $I_{(\mathrm{hk}),\mathrm{ref}}$ is the intensity that would be measured if the temperature were the same as before excitation. We write $I_{(\mathrm{hk}),\mathrm{ref}} = I_{(\mathrm{hk}),\mathrm{ref}}(t)$ to indicate that measured intensities might be subject to small temporal variations due to instabilities in the experimental setup. With $(G_{(11)}/G_{(10)})^2 = 3$ for graphene and $\Delta\tilde{T}_\mathrm{l} = p(T_\mathrm{l} - T_{\mathrm{l,ref}})G_{(10)}^2$, Supplementary Equations 4 and 5 are rewritten as:

$$\frac{I_{(10)}(t)}{I_{(10),\mathrm{ref}}(t)} = exp(-\Delta\tilde{T}_\mathrm{l}(t)) \quad (6)$$

$$\frac{I_{(11)}(t)}{I_{(11),\mathrm{ref}}(t)} = exp(-3\,\Delta\tilde{T}_\mathrm{l}(t)) \quad (7)$$

$\Delta\tilde{T}_\mathrm{l}$ and the temperature change $\Delta T_\mathrm{l} = T_\mathrm{l} - T_{\mathrm{l,ref}}$ are related by a constant factor, $pG_{[10]}^2$. Thus, $\Delta\tilde{T}_\mathrm{l}$ can be considered as the temperature change measured in special units. In the following $\Delta\tilde{T}_\mathrm{l}$ will be identified with ΔT_l. Hence, the relative intensity changes ($I_{(\mathrm{hk})}/I_{(\mathrm{hk}),\mathrm{ref}}$) of the 1st and 2nd order reflection due to the Debye-Waller effect are related to the change in lattice temperature according to

$$x_{(10),\mathrm{DW}} = exp(-\Delta T_\mathrm{l}(t)) \quad (8)$$

$$x_{(11),\mathrm{DW}} = exp(-3\,\Delta T_\mathrm{l}(t)) \quad (9)$$

In order to describe the variation of the lattice temperature after photo-excitation, first a simple model was used based on the assumption of a thermal system in contact with a heat bath at temperature $T_{\mathrm{l,ref}}$ which absorbs a certain amount of energy E at time t_0. In this simplest version, the absorbed energy is immediately converted to thermal energy, leading to a sudden rise in temperature of $\Delta T = E/C$ at $t = 0$ where C is the lattice heat capacity. At $t > 0$ the temperature excursion decays exponentially via anharmonic phonon coupling modes of graphene if the thermal relaxation rate, b_T, is constant (*1*). This model already captures the most important features of the temperature curve, and the measured intensity traces can be fitted with this model to fairly high quality if the temporal resolution of the measurements is taken into account (see

Supplementary Note 5). However, conversion of absorbed energy into lattice vibrations corresponding to a Boltzmann distribution at elevated temperature proceeds on time scales comparable to the temporal resolution, on the order of a few picoseconds (*1*). To allow for a gradual increase of the temperature after photo-excitation we finally used a combination of two exponentials of the form:

$$\Delta T_{\mathrm{l}}(t) = X_{\mathrm{T}}(exp(-a_{\mathrm{T}}t) - exp(-b_{\mathrm{T}}t))\left(\frac{a_{\mathrm{T}}}{b_{\mathrm{T}}-a_{\mathrm{T}}}\right)\Theta(t) \qquad (10)$$

Here, X_{T} is a constant, a_{T} and b_{T} are rate constants describing the gradual conversion of the absorbed energy into lattice vibrations and the relaxation back to equilibrium by thermal transfer to the heat bath. Θ is the Heaviside step function. Supplementary Equation 10 is the solution of the inhomogeneous differential equation:

$$C\,\frac{dT_{\mathrm{l}}}{dt} = \Delta E\; a_{\mathrm{T}}\; \exp(-a_{\mathrm{T}}\,t) - C\; b_{\mathrm{T}}\,(T_{\mathrm{l}} - T_{\mathrm{ref}}) \qquad (11)$$

Solving Supplementary Equation 11 shows that $X_{\mathrm{T}} = E/C$. This is the maximum lattice temperature that could be reached after long time if thermal relaxation were forbidden ($b_{\mathrm{T}} = 0$). Thus, X_{T} should be proportional to the fluence used in the experiments, and the adequacy of the model can be measured against the degree of proportionality.

The first term in Supplementary Equation 11 describes the conversion of absorbed energy into lattice heat. It is modelled as an exponential decay that is independent of the lattice temperature. More complicated models with a higher number of free parameters could be envisioned. However, the number of parameters that can be determined by fitting to the observed intensity traces is limited by the precision of the experimental data.

Note 4: Surface field effect.

For the quantitative analysis of the measured intensity kinetics of the projection images, a phenomenological approach was adopted due to the lack of a comprehensive physical model of space charge dominated plasma dynamics, comprising both the initial plasma build-up and the subsequent charge recombination process. We used a two-exponential function similar to Supplementary Equation 10 to express x_{SF} as a function of time:

$$x_{\mathrm{SF}}(t) = 1 - X_{\mathrm{SF}}(exp(-a_{\mathrm{SF}}\,t) - exp(-b_{\mathrm{SF}}\,t))\left(\frac{a_{\mathrm{SF}}}{b_{\mathrm{SF}}-a_{\mathrm{SF}}}\right)\Theta(t) \qquad (12)$$

The form of the exponential term in Supplementary Equation 12 is the same as that used to model the temperature variation underlying the Debye-Waller effect. By analogy to X_{T}, the constant factor X_{SF} can be used to quantify the overall strength of the surface field effect. The terms a_{SF} and b_{SF} are the rate constants of the build-up and the decay phase of the surface field effect. Supplementary Equation 12 is well-suited for characterizing the observed initial intensity drop and the subsequent recovery observed in projection imaging.

Note 5: Convolution with probe pulse.

The observed intensity time traces are blurred by the finite temporal resolution of the measurements which is mainly determined by the probe electron bunch duration (≅ 12 ps FWHM for the *D* = 180 fs excitation case), longer than the delay time interval (≅ 3.3 ps). Hence, functions x_{SF} (direct beam case) or $x_{\mathrm{SF}}\,x_{(\mathrm{hk}),\mathrm{DW}}$ (diffraction experiments) were transformed by

numerical convolution with the pulse profile, before comparing them with measurements of the relative intensities I/I_{ref}. A Gaussian profile P_{σ_e} with standard deviation $\sigma_\mathrm{e} = 5$ ps = FWHH/2.355 was assumed.

$$y_{\mathrm{obs}}(t) = \frac{I(t)}{I_{\mathrm{ref}}(t)} = \left[x_{\mathrm{SF}} * P_{\sigma_\mathrm{e}}\right](t) + \varepsilon(t) \quad (13)$$

$$y_{(\mathrm{hk}),\mathrm{obs}}(t) = \frac{I_{(\mathrm{hk})}(t)}{I_{(\mathrm{hk}),\mathrm{ref}}(t)} = \left[x_{\mathrm{SF}}\, x_{(\mathrm{hk}),\mathrm{DW}} * P_{\sigma_\mathrm{e}}\right](t) + \varepsilon_{(\mathrm{hk})}(t) \quad (14)$$

In these preliminary equations, the asterisk denotes convolution, $y_{\mathrm{obs}}(t)$ the observed data, and $\varepsilon(t)$ deviations from the expected values due to statistical errors of the measurements (residuals). In the absence of systematic errors, deviations from the expected values should be distributed about zero. In this case, Supplementary Equations 13 and 14 could be used to fit the free parameters that appear on the right side by minimizing the sum of the squared residuals.

Note 6: Intensity drift correction.

According to Supplementary Equations 13 and 14 the relative intensities measured at negative times should be distributed around 1 because $y_{\mathrm{obs}}(t) = 1 + \varepsilon(t)$ for $t \ll -\sigma_\mathrm{e}$. However, this was not the case in general, indicating that small systematic errors remained even after careful correction of the raw data (see Supplementary Note 1). To account for such errors, the fit function was modified by addition of a "drift" term in the form of a Taylor expansion, $y_0 + y_1 t + y_2\, t^2$ ..., where the parameters y_i were considered as fit parameters. For some of the direct beam traces, inclusion of terms up to second order in t led to small improvements of the fit. However, in order to reduce the danger of overfitting, the expansion was generally truncated at the linear term. In most cases, and in particular for all traces of the diffraction experiments, inclusion of the constant term was sufficient to obtain satisfying results. Thus, the final form of the fit function was

$$y_{\mathrm{calc}}(t) = \left[x_{\mathrm{SF}} * P_{\sigma_\mathrm{e}}\right](t) + y_0 + y_1 t \quad \text{(for surface field effect)} \quad (15)$$

$$y_{(\mathrm{hk}),\mathrm{calc}}(t) = \left[x_{\mathrm{SF}}\, x_{(\mathrm{hk}),\mathrm{DW}} * P_{\sigma_\mathrm{e}}\right](t) + y_{(\mathrm{hk}),0} \quad \text{(for Debye-Waller effect)} \quad (16)$$

with $y_1 = 0$ for all but two cases (see Supplementary Table 1).

Note 7: Procedure of fitting.

First, the traces of the direct beam experiments were fitted using Supplementary Equation 15 with 5 or 6 parameters $(t_0, X_{\mathrm{SF}}, a_{\mathrm{SF}}, b_{\mathrm{SF}}, y_0\ [, y_1])$, in general. Measured traces and fitted curves are shown in Supplementary Figure 3, and the fitted parameters are listed in Supplementary Table 1. It turned out that the rate constants a_{SF} $(= 1/\tau_{\mathrm{SF,ini}})$ and b_{SF} $(= 1/\tau_{\mathrm{SF,rec}})$ did not vary a lot for conditions where the surface field effect is strong and contamination of diffraction data is high. Thus, when the diffraction data were fitted, a_{SF} and b_{SF} were set to the mean values of the results obtained from the direct beam experiments, in order to reduce the number of free parameters. The diffraction data were fitted using Supplementary Equation 16, with up to 7 free parameters $(t_0, X_{\mathrm{T}}, a_{\mathrm{T}}, b_{\mathrm{T}}, X_{\mathrm{SF}}, y_{(10),0}, y_{(11),0})$. The traces of both diffraction orders were fitted simultaneously by minimizing the total sum of the squared residuals. The results are presented in Supplementary Figure 6 and Supplementary Table 3 (with $a_{\mathrm{T}} = 1/\tau_{\mathrm{T,ini}}$ and $b_{\mathrm{T}} = 1/\tau_{\mathrm{T,rec}}$). It should be noted that the surface field effect was assumed to be the same for both diffraction

orders. The results of the *D*-series showed that the SF effect is negligible at *F* of 12.1 mJ/cm² and *D* of 2 ps and above. In the *F*-series, *D* was 2 ps, and *F* did not exceed 12.1 mJ/cm². Hence, for the final calculations, parameter X_{SF} was set to zero (for the *F*-series), reducing the number of free parameters from 7 to 6. Calculations were done with R (*2*), and R package minpack.lm (*3*) was used for non-linear least-squares fitting with the Levenberg-Marquardt algorithm.

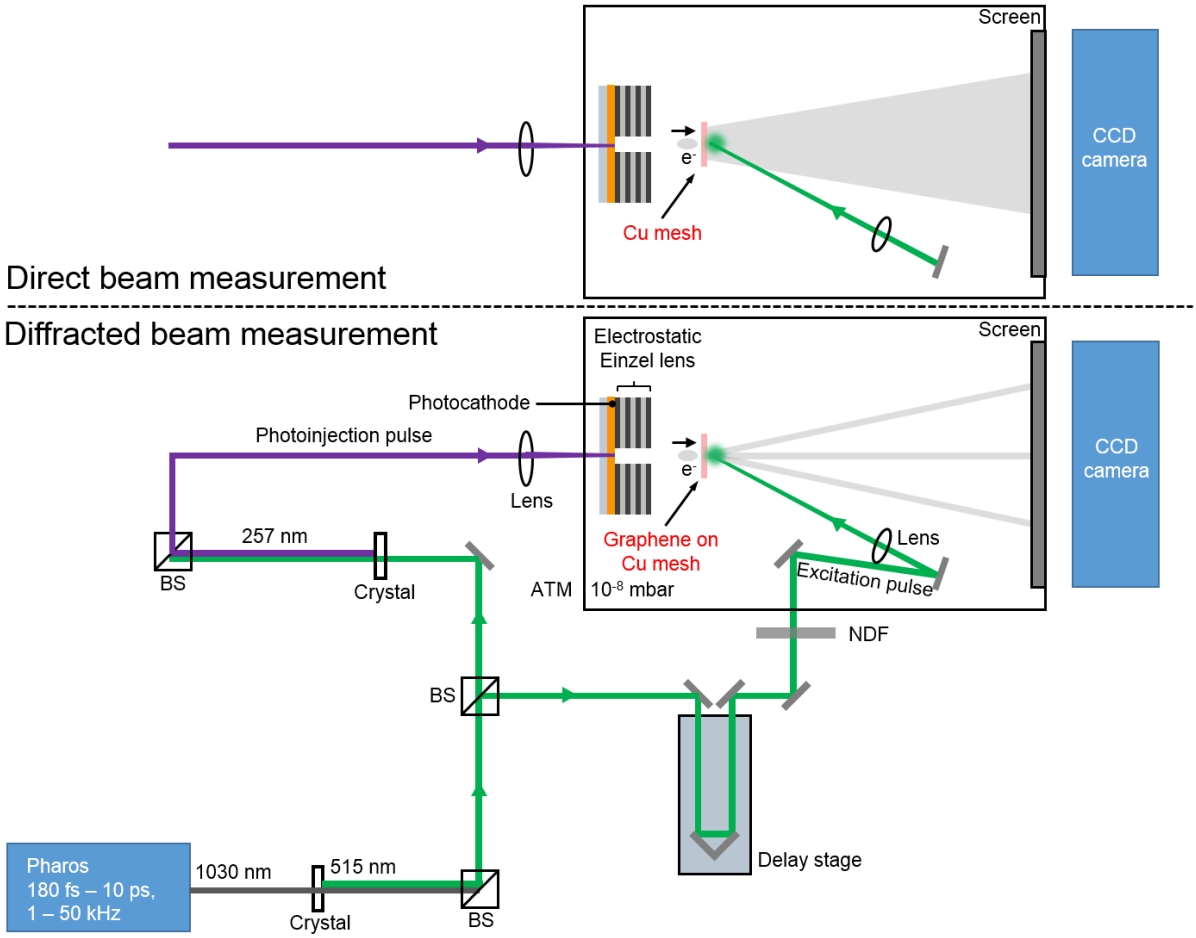

Supplementary Figure 1. Schematic of the experimental setup. The master laser system used in the present work was a Yb:KGW based femtosecond laser system (Pharos, Light Conversion) operating at 1030 nm central wavelength with tunable pulse duration (180 fs – 10 ps) and repetition rate (1 – 50 kHz). The fundamental laser pulse was frequency-doubled to generate a second harmonic (515 nm) split (by a beam splitter, BS) into two arms. One arm was frequency-doubled to obtain a fourth harmonic (257 nm) that is back-illuminating the photocathode to generate an electron bunch. A stack of metal and insulator plates is directly integrated to the photocathode, used as an electrostatic Einzel lens for the purpose of electron bunch focusing. The other arm was the excitation source that irradiates the sample after going through a focusing lens, with an incident angle of approximately 30°. The excitation laser fluence was adjusted by manually rotating the neutral density filter (NDF) wheel, and the pulse duration was changed by computer-controlled variation of the separation distance of a grating pair built into the laser system. The adjusted fluence and the pulse duration were independently confirmed by a laser power measurement and by an autocorrelation measurement, respectively. The time-delay between the electron bunch and the excitation pulse was varied over the desired range by a programmed scan of the retroreflector position on the delay line stage. After passing the sample, direct and diffracted electrons are collected at a microchannel plate (chevron type, pore diameter: 12 μm)/phosphor screen assembly inside a vacuum chamber (~1×10^{-8} mbar), and electron images are recorded with a scientific grade CCD camera (PI system, Ropers scientific Ltd.)

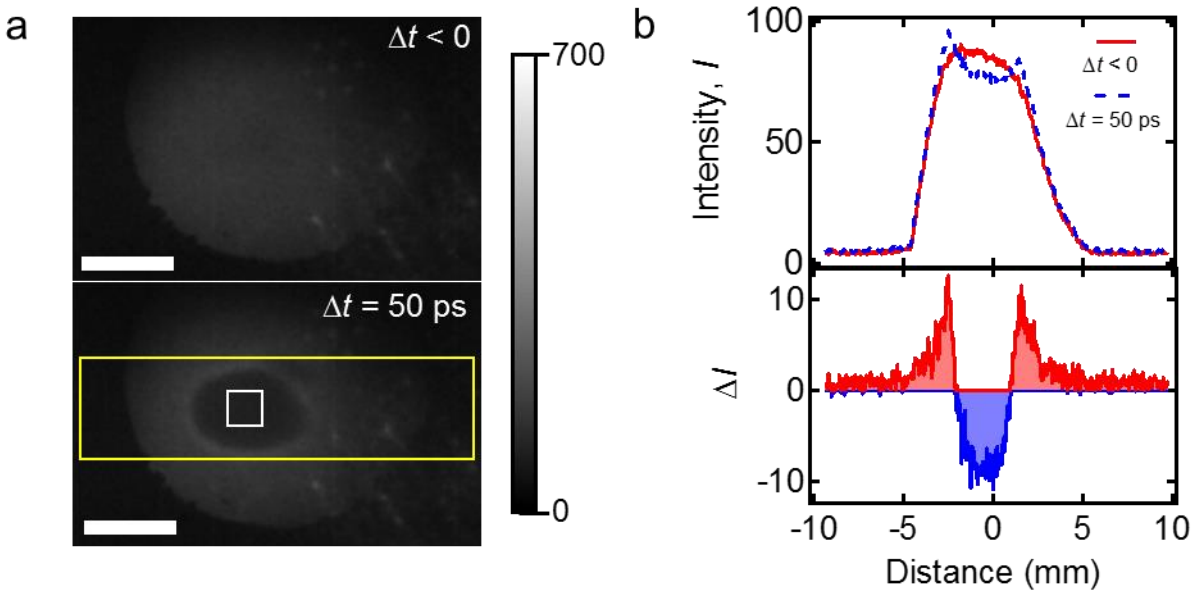

Supplementary Figure 2. Direct beam image analysis. a Typical projection image of the copper mesh grid before (upper panel) and after (lower panel) excitation. The kinetic energy of the probe electron for this measurement was 0.5 keV. Scale bar is 5 mm. **b** Line profiles (upper graph) of a region-of-interest (indicated by the opened yellow box) of the direct beam image in Supplementary Fig. 2a. The profiles are integrated in the horizontal direction. The lower graph shows the difference of the profiles between the projection images. The sum of the red and blue shaded area is equal to 0, indicating the conservation of the total charge of the probe electron bunch.

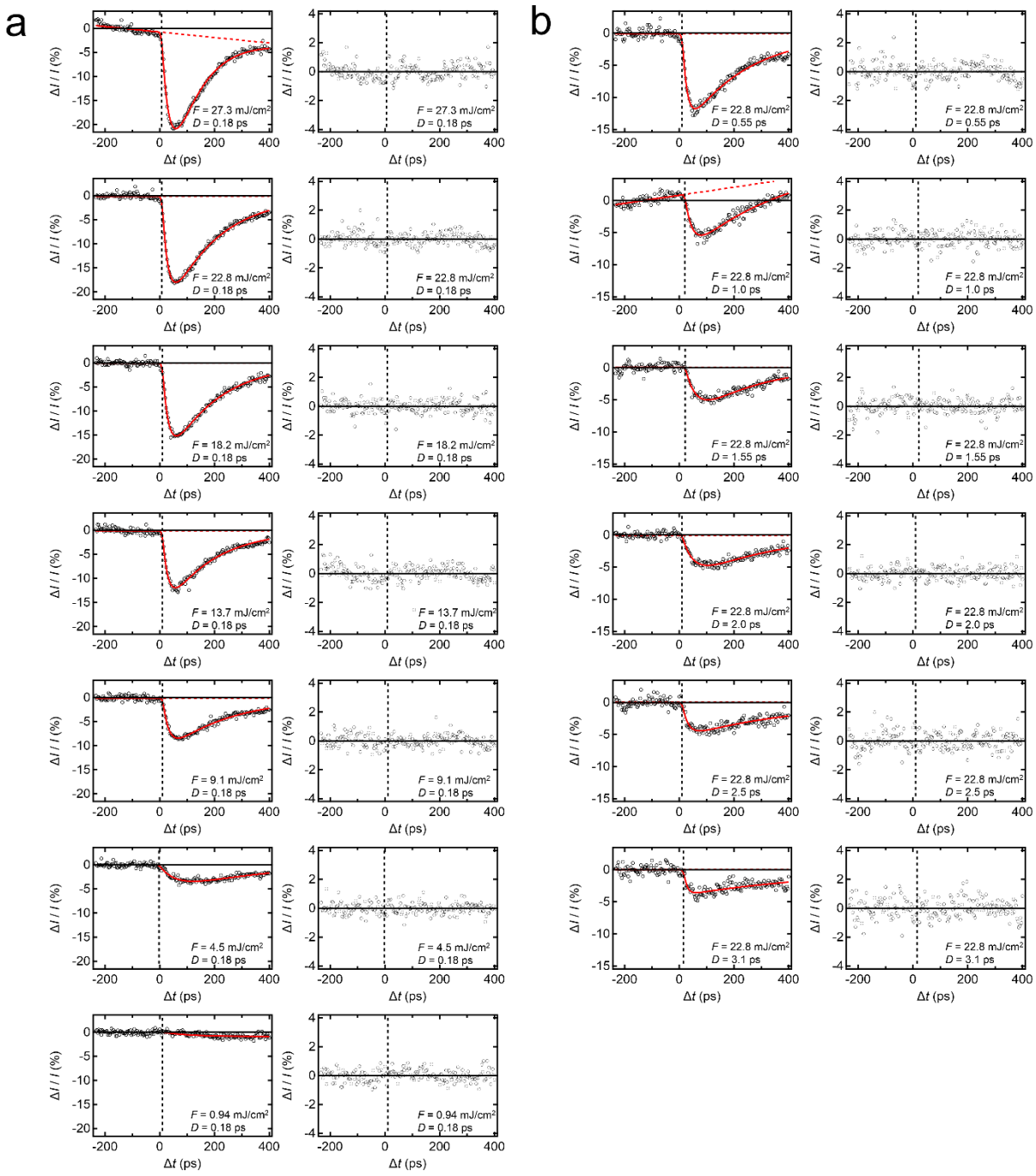

Supplementary Figure 3. *F*- and *D*-dependent pump-probe kinetics of the direct beam intensity. a *F*-dependence. Black circles in the left plots are the measured intensity changes, $\Delta I/I$, as a function of Δt, and the solid red curve corresponds to the fit of each time-trace. Dotted black and red lines indicate the correction of the intensity drift and the time zero shift, respectively. The right plots are the corresponding residual values from the two-exponential model used to fit the data (for details see Supplementary Note 2). **b** *D*-dependence.

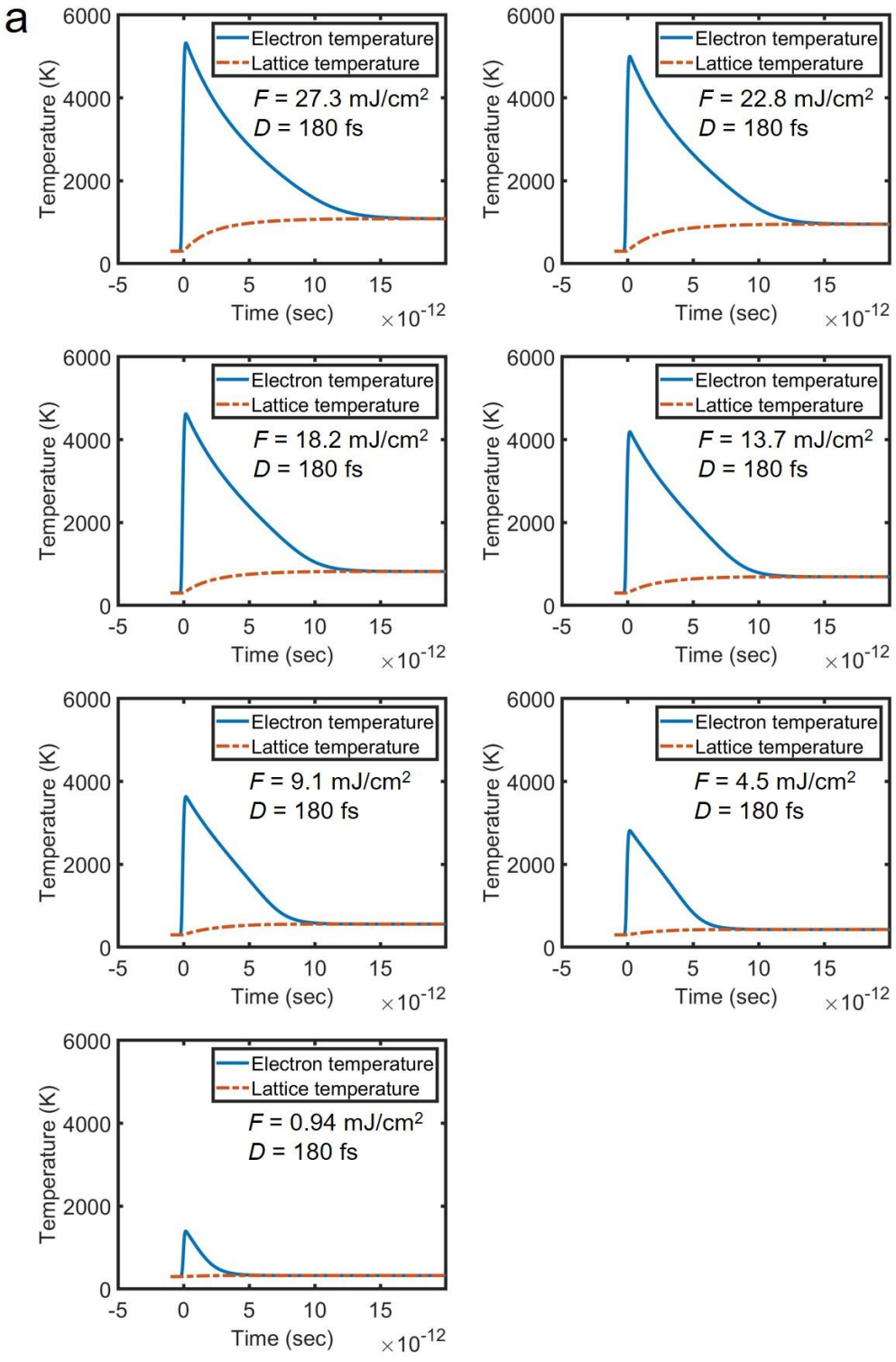
a
Electron temperature
Lattice temperature
F = 27.3 mJ/cm2
D = 180 fs
F = 22.8 mJ/cm2
D = 180 fs
F = 18.2 mJ/cm2
D = 180 fs
F = 13.7 mJ/cm2
D = 180 fs
F = 9.1 mJ/cm2
D = 180 fs
F = 4.5 mJ/cm2
D = 180 fs
F = 0.94 mJ/cm2
D = 180 fs
Temperature (K)
Time (sec)
×10-12

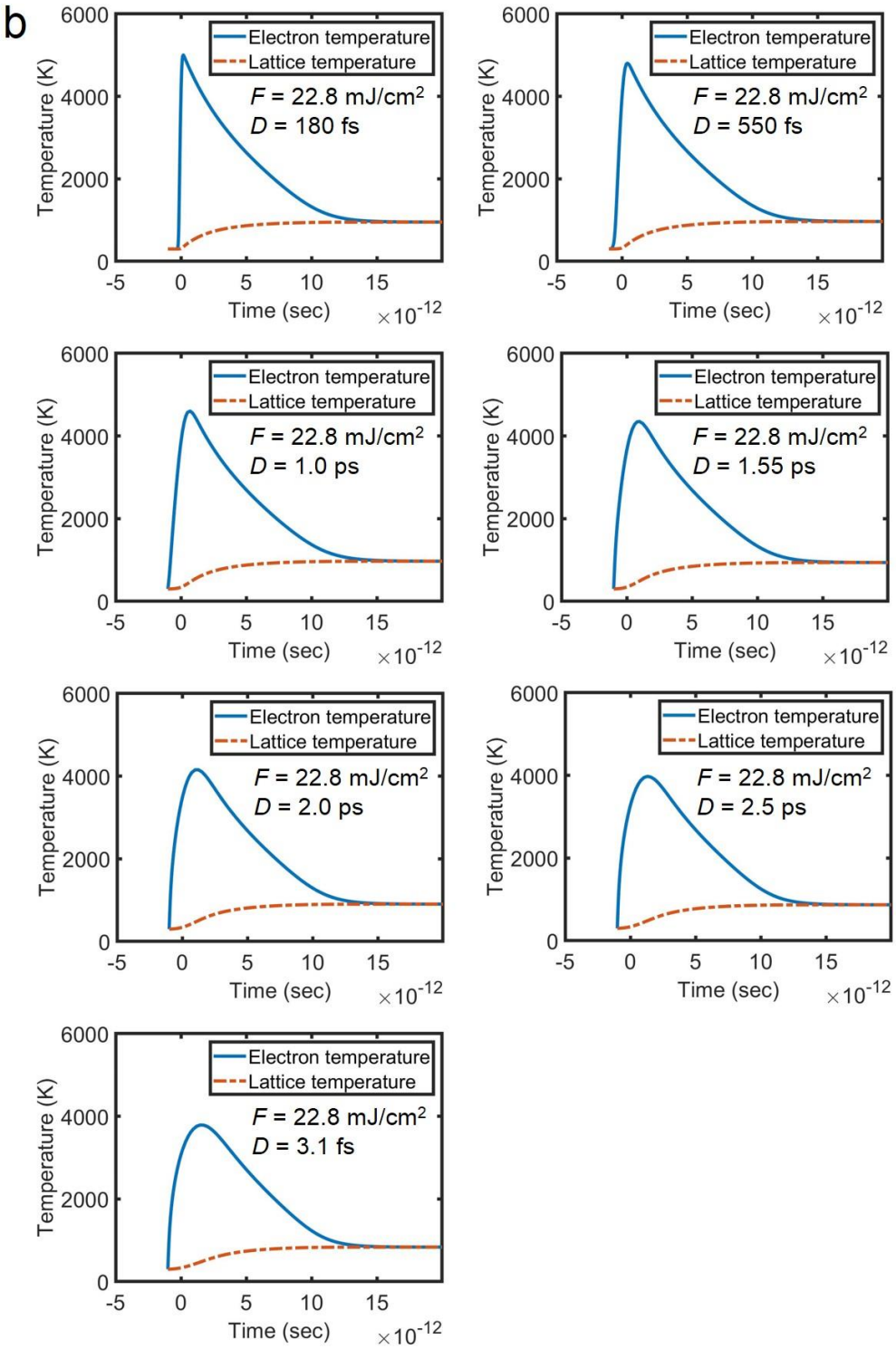

Supplementary Figure. 4. Calculated temporal evolution of electronic and lattice temperature of the Cu mesh. a *F*-dependence: profiles at a fixed *D* of 180 fs and varying *F*s. **b** *D*-dependence: profiles at a fixed *F* of 22.8 mJ/cm^2 and varying *D*s.

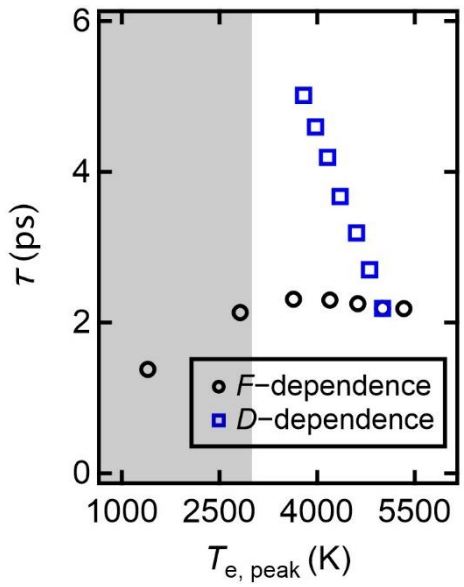

Supplementary Figure 5. Relation between $T_{e,peak}$ and τ of the Cu mesh upon excitation with different *F* and *D*. The values are tabulated in Supplementary Table 1.

a

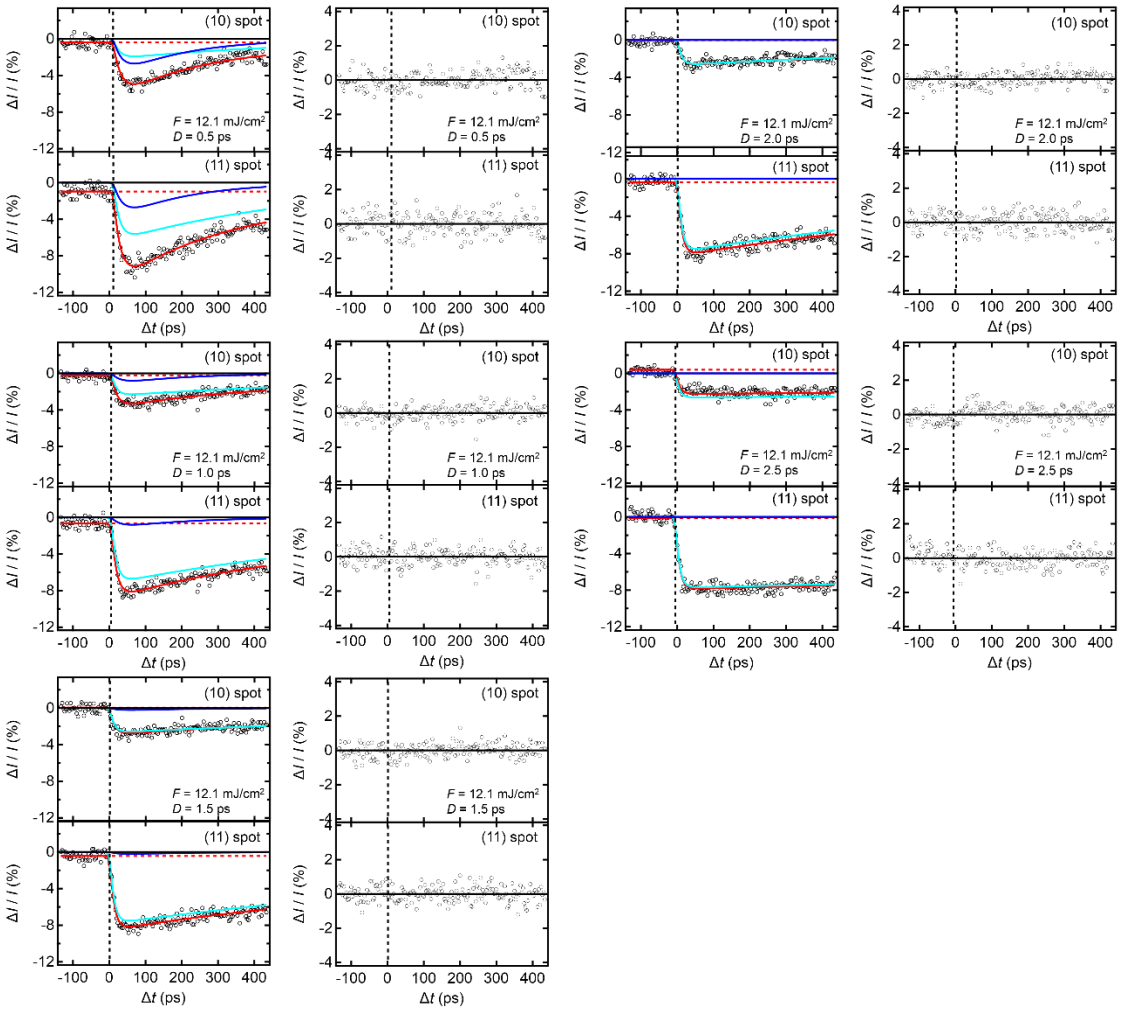
(10) spot
(11) spot
F = 12.1 mJ/cm²
D = 0.5 ps
D = 1.0 ps
D = 1.5 ps
D = 2.0 ps
D = 2.5 ps
Δt (ps)
Δ I / I (%)

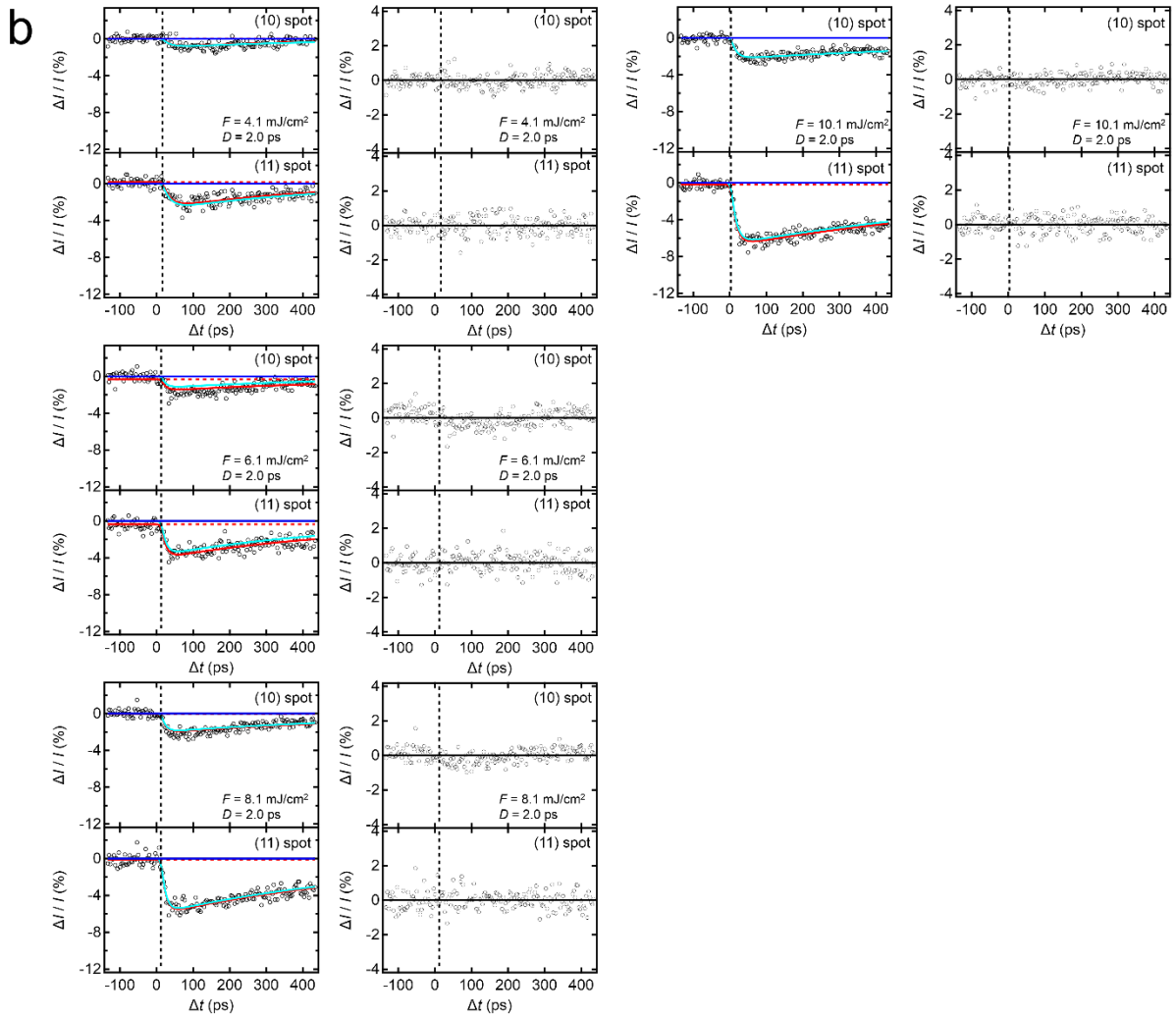

Supplementary Figure 6. *F*- and *D*-dependent pump-probe kinetics of diffracted beam intensities. a *D*-dependence. Black circles in the left plot are the relative intensity changes, $\Delta I/I$, of the (10) reflections (upper panel) and the (11) reflections (bottom panel), and the solid red curves are the results of simultaneous fits of both traces. Surface field and Debye-Waller effects are depicted separately by solid blue and cyan curves, respectively. Dotted red and black lines indicated intensity offsets and the time zero shifts. Plots on the right side show the corresponding residuals. **b** *F*-dependence.

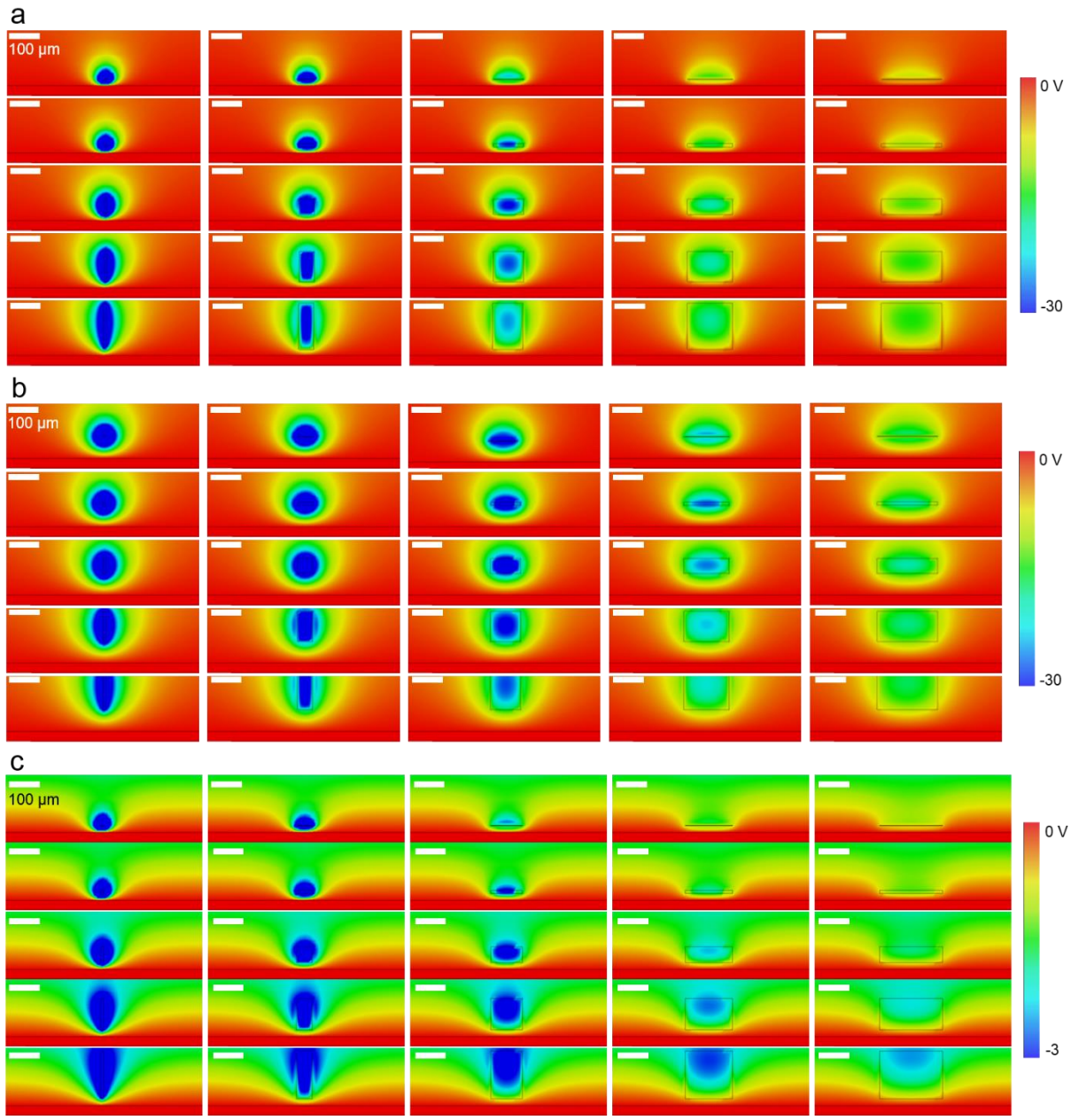

Supplementary Figure 7. Calculated electric potential distribution at the charge separated region. a-c The plasma charge is set to (160 fC, d = 20 μm) (**a**), (160 fC, d = 70 μm) (**b**), and (16 fC, d = 20 μm) (**c**), respectively. φ = 10, 50, 100, 150, 200 μm (from left to right), δ = 1, 10, 50, 100, 150 μm (from top to bottom).

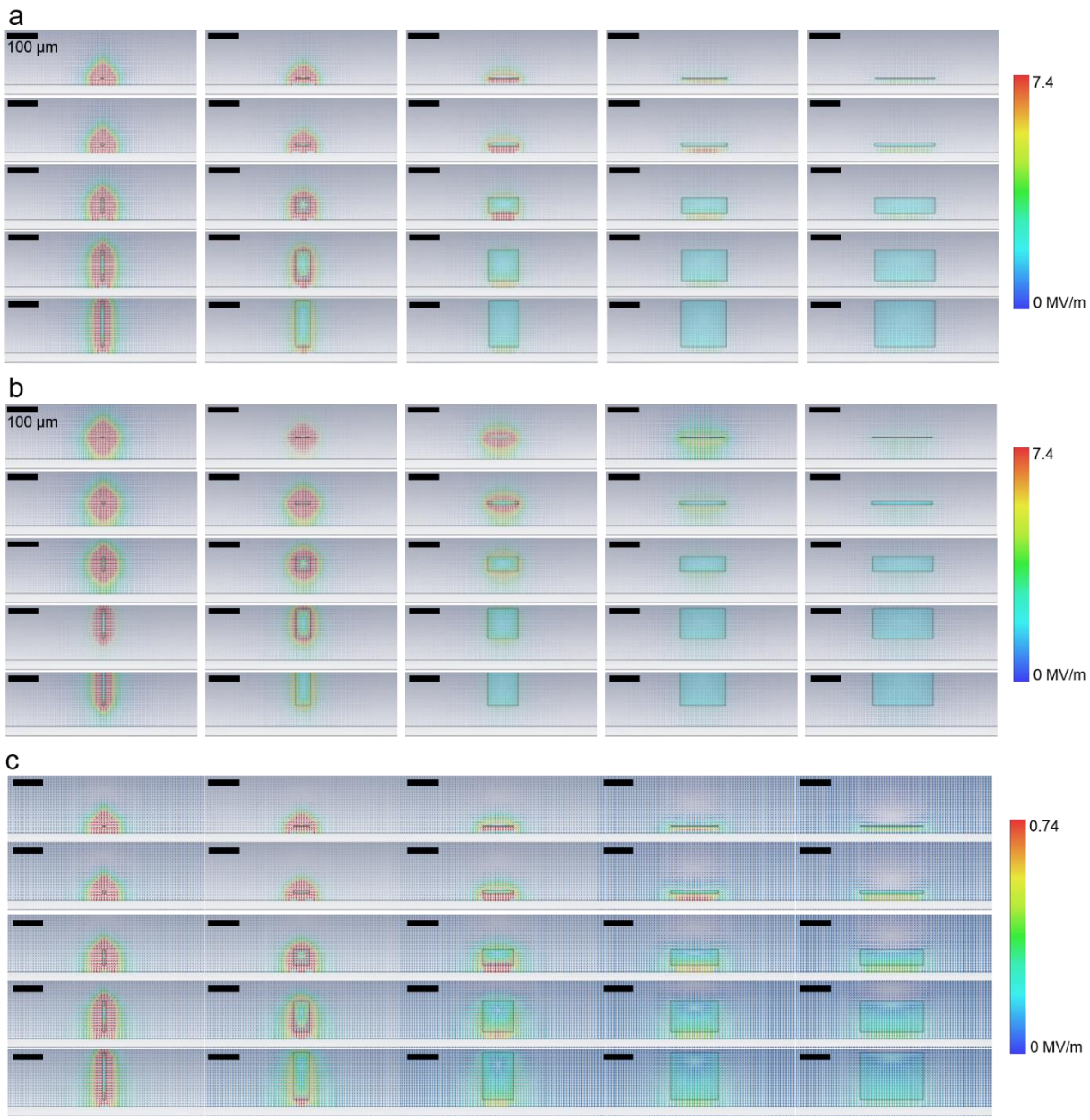

Supplementary Figure 8. Calculated electric field at the charge separated region. a-c The plasma charge is set to (160 fC, d = 20 μm) (**a**), (160 fC, d = 70 μm) (**b**), and (16 fC, d = 20 μm) (**c**), respectively. From left to right: φ = 10, 50, 100, 150, 200 μm, from top to bottom: δ = 1, 10, 50, 100, 150 μm.

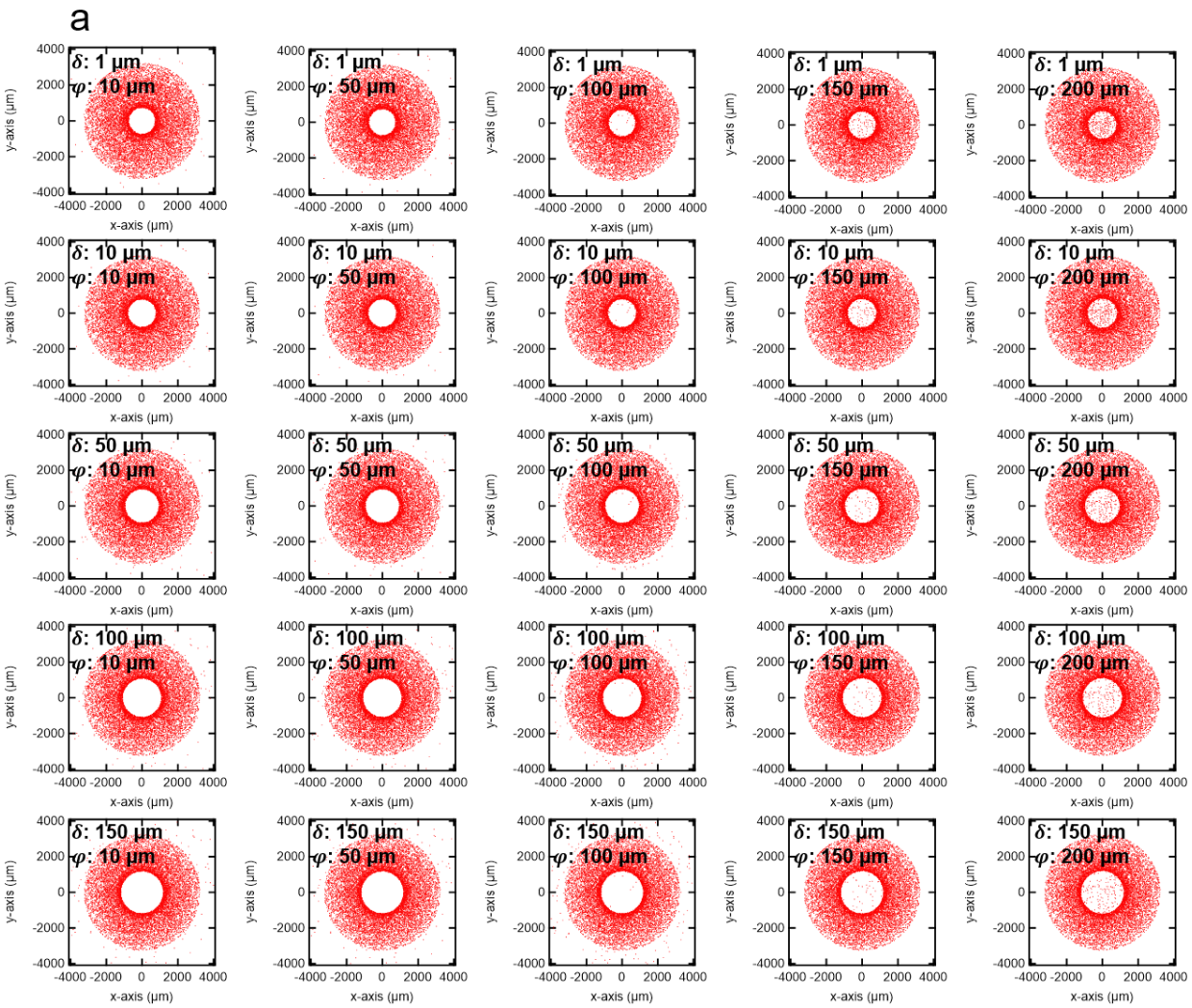
a
δ: 1 μm
φ: 10 μm
δ: 1 μm
φ: 50 μm
δ: 1 μm
φ: 100 μm
δ: 1 μm
φ: 150 μm
δ: 1 μm
φ: 200 μm
δ: 10 μm
φ: 10 μm
δ: 10 μm
φ: 50 μm
δ: 10 μm
φ: 100 μm
δ: 10 μm
φ: 150 μm
δ: 10 μm
φ: 200 μm
δ: 50 μm
φ: 10 μm
δ: 50 μm
φ: 50 μm
δ: 50 μm
φ: 100 μm
δ: 50 μm
φ: 150 μm
δ: 50 μm
φ: 200 μm
δ: 100 μm
φ: 10 μm
δ: 100 μm
φ: 50 μm
δ: 100 μm
φ: 100 μm
δ: 100 μm
φ: 150 μm
δ: 100 μm
φ: 200 μm
δ: 150 μm
φ: 10 μm
δ: 150 μm
φ: 50 μm
δ: 150 μm
φ: 100 μm
δ: 150 μm
φ: 150 μm
δ: 150 μm
φ: 200 μm
x-axis (μm)
y-axis (μm)
4000
2000
0
-2000
-4000

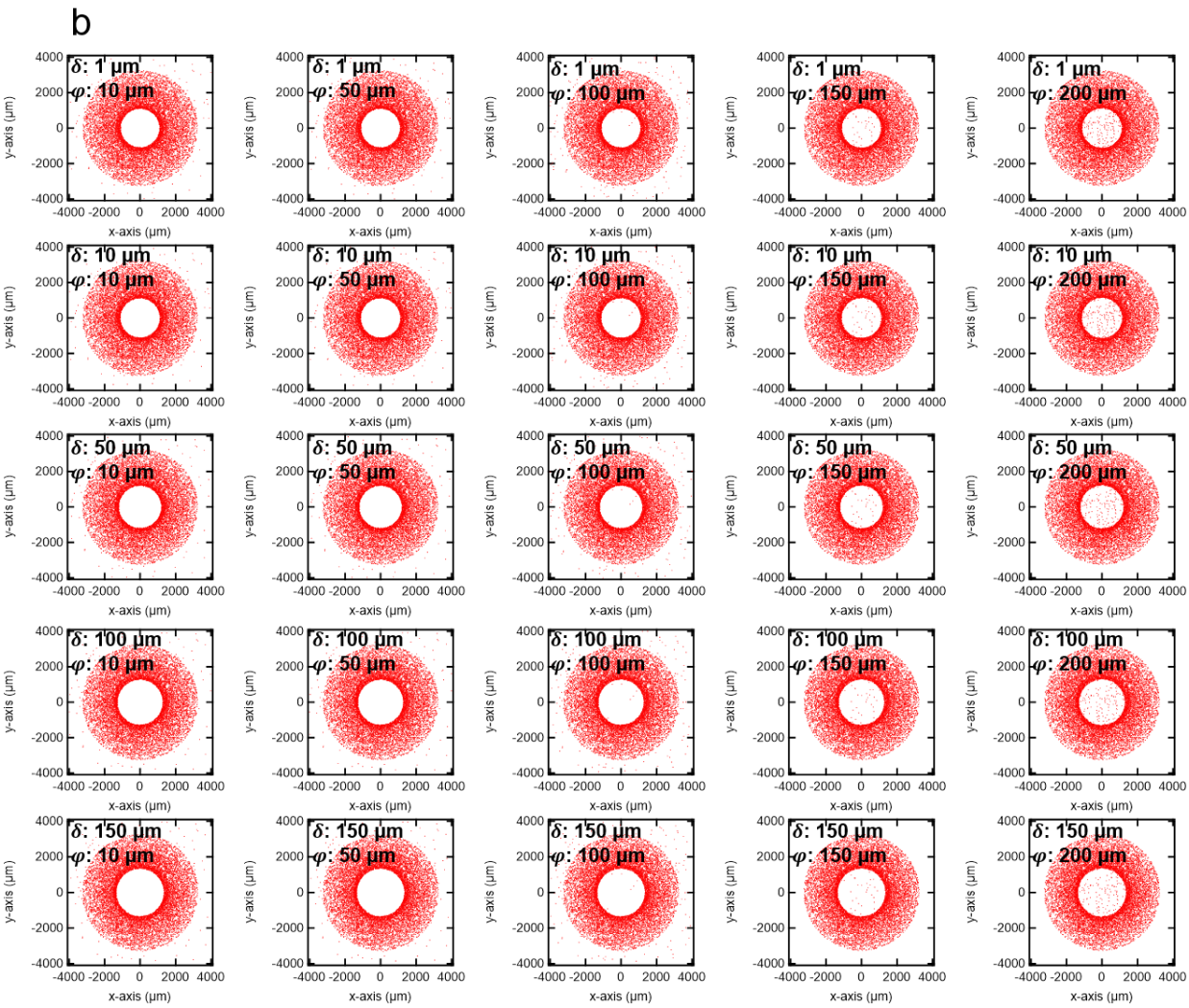
b
δ: 1 μm
φ: 10 μm
δ: 1 μm
φ: 50 μm
δ: 1 μm
φ: 100 μm
δ: 1 μm
φ: 150 μm
δ: 1 μm
φ: 200 μm
δ: 10 μm
φ: 10 μm
δ: 10 μm
φ: 50 μm
δ: 10 μm
φ: 100 μm
δ: 10 μm
φ: 150 μm
δ: 10 μm
φ: 200 μm
δ: 50 μm
φ: 10 μm
δ: 50 μm
φ: 50 μm
δ: 50 μm
φ: 100 μm
δ: 50 μm
φ: 150 μm
δ: 50 μm
φ: 200 μm
δ: 100 μm
φ: 10 μm
δ: 100 μm
φ: 50 μm
δ: 100 μm
φ: 100 μm
δ: 100 μm
φ: 150 μm
δ: 100 μm
φ: 200 μm
δ: 150 μm
φ: 10 μm
δ: 150 μm
φ: 50 μm
δ: 150 μm
φ: 100 μm
δ: 150 μm
φ: 150 μm
δ: 150 μm
φ: 200 μm
x-axis (μm)
y-axis (μm)
4000
2000
0
-2000
-4000

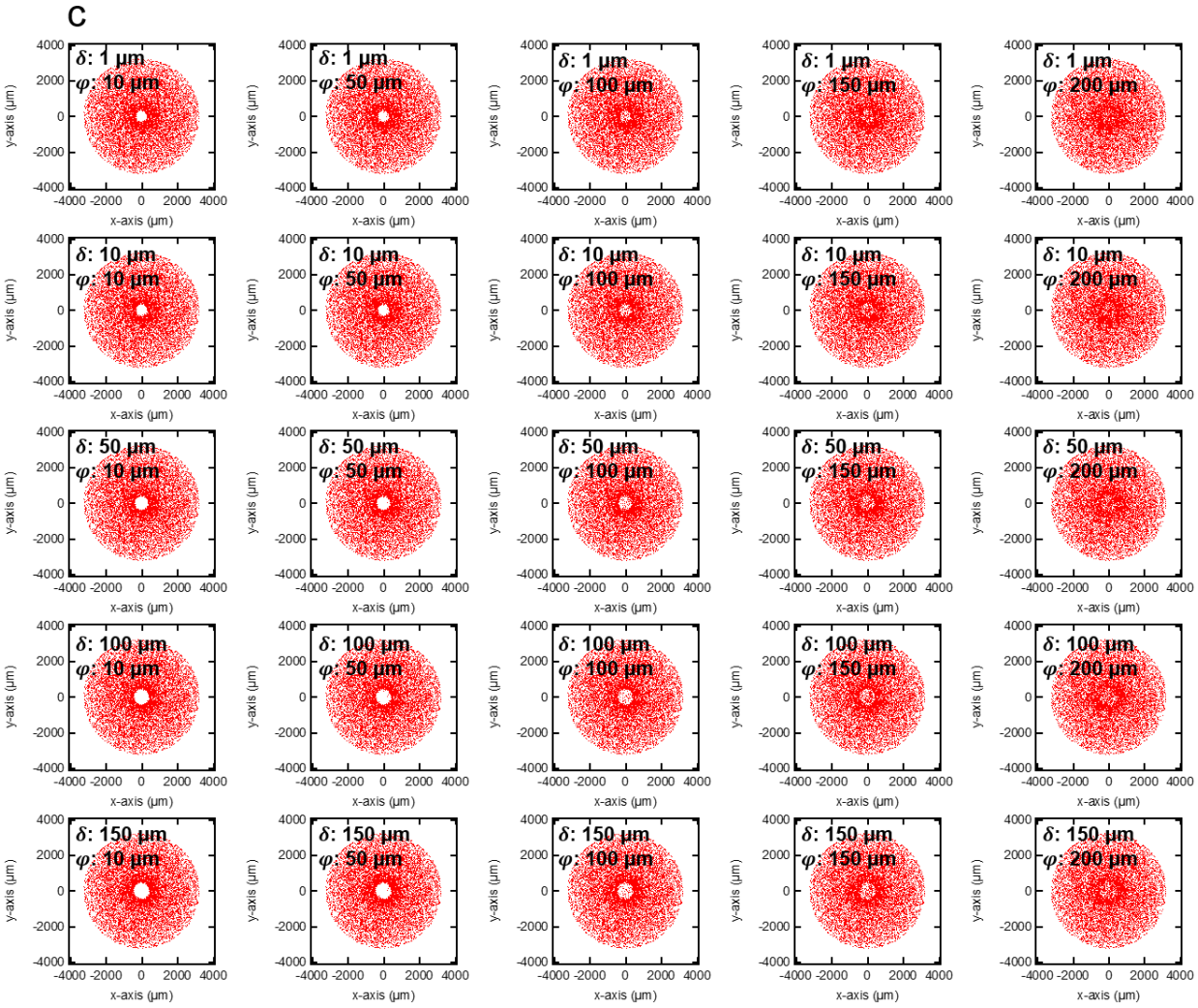

Supplementary Figure 9. Distribution of final positions of low-energy electrons at the screen plane. a-c The plasma charge is set to (160 fC, d = 20 μm) (a), (160 fC, d = 70 μm) (b), and (16 fC, d = 20 μm) (c), respectively.

F (mJ/cm^2)	t_0 (ps)	$100\ X_{SF}$	$\tau_{SF,ini}$ (ps)	$\tau_{SF,rec}$ (ps)	$10^4\ y_0$	$10^6\ y_1$
0.94*	10.0	0.9 ±0.1	100	∞	2.7 ±4.3	0
4.5	-2.8 ±3.0	5.2 ±0.5	64.5 ±11.6	294.8 ±45.0	-1.3 ±4.6	0
9.1	10.2 ±1.0	10.6 ±0.2	21.4 ±1.6	227.5 ±7.1	-8.9 ±5.0	0
13.7	8.8 ±0.8	15.7 ±0.3	19.2 ±1.3	170.0 ±4.4	-11.5 ±5.9	0
18.2	9.0 ±0.5	20.2 ±0.2	20.9 ±0.9	177.6 ±3.2	-4.8 ±5.2	0
22.8	7.7 ±0.4	23.8 ±0.2	20.5 ±0.8	177.8 ±2.7	-9.2 ±5.2	0
27.3	6.2 ±0.5	31.8 ±0.7	28.0 ±1.5	107.6 ±4.4	-77.6 ±7.0	57.0 ±4.1
D (ps)	t_0 (ps)	$100\ X_{SF}$	$\tau_{SF,ini}$ (ps)	$\tau_{SF,rec}$ (ps)	$10^4\ y_0$	$10^6\ y_1$
0.18	7.7 ±0.4	23.8 ±0.2	20.5 ±0.8	177.8 ±2.7	-9.2 ±5.2	0
0.55	10.2 ±0.9	14.4 ±0.2	17.0 ±1.4	222.5 ±6.4	-10.5 ±6.8	0
1.0	19.6 ±1.5	8.7 ±0.3	25.3 ±3.0	255.8 ±30.7	82.3 ±9.4	62.9 ±7.0
1.55	21.7 ±2.1	7.4 ±0.4	39.2 ±5.4	219.7 ±18.3	7.2 ±5.8	0
2.0	9.3 ±2.0	6.5 ±2.7	40.4 ±4.7	303.0 ±23.4	4.2 ±4.9	0
2.5	9.6 ±2.7	5.2 ±0.2	21.0 ±4.4	405.5 ±40.2	-2.2 ±7.1	0
3.1	15.0 ±3.4	3.9 ±0.2	11.7 ±4.6	526.9 ±72.6	-1.9 ±7.6	0

Supplementary Table 1. Summary of fitted parameters for the direct beam case. These parameters are determined by the two-exponential model. The error values correspond to ±1 standard deviation. *The F = 0.94 mJ/cm² trace was fitted with two free parameters, all other parameters were set to fixed values. Due to the low S/N of this trace, $\boldsymbol{X_{SF}}$ is the only parameter that can be fitted with reasonable confidence.

F (mJ/cm^2)	D (fs)	$T_{\mathrm{e,peak}}$ (K)	τ (ps)
27.3	180	5331.6	2.185
22.8	180	5004.3	2.188
18.2	180	4624.7	2.251
13.7	180	4194.4	2.298
9.1	180	3636.3	2.310
4.5	180	2817.4	2.133
0.94	180	1398.4	1.378
22.8	550	4805.4	2.701
22.8	1000	4605	3.189
22.8	1550	4352.3	3.671
22.8	2000	4159.7	4.191
22.8	2500	3975.1	4.595
22.8	3100	3791.5	5.015

Supplementary Table 2. Summary of $\boldsymbol{T_{\mathrm{e,peak}}}$ and $\boldsymbol{\tau}$ of the Cu mesh upon excitation with different $\boldsymbol{F}$ and $\boldsymbol{D}$. These values are determined from the calculated electronic temperature profile, $\boldsymbol{T_{\mathrm{e}}}(\Delta \boldsymbol{t})$, in Supplementary Fig. 4.

F (mJ/cm^2)	t_0 (ps)	X_T	$\tau_{T,ini}$ (ps)	$\tau_{T,rec}$ (ps)	$y_{(10),0}$	$y_{(11),0}$	X_{SF}
12.1	1.2 ±0.7	2.7E-02 ±4.1E-04	10.3 ±1.1	1199 ±80	-2.4E-04 ±4.0E-04	-3.9E-03 ±6.7E-04	0
10.1	2.9 ±0.7	2.3E-02 ±4.0E-04	13.9 ±1.2	915 ±57	-7.9E-05 ±3.6E-04	-2.0E-03 ±6.1E-04	0
8.1	12.0 ±0.9	2.0E-02 ±4.5E-04	11.4 ±1.5	628 ±39	-7.1E-04 ±4.1E-04	-1.1E-03 ±6.8E-04	0
6.1	12.5 ±1.5	1.2E-02 ±5.0E-04	11.8 ±2.7	501 ±49	-3.2E-03 ±4.5E-04	-3.6E-03 ±7.4E-04	0
4.1	15.9 ±2.5	9.1E-03 ±5.0E-04	21.3 ±4.6	430 ±52	4.0E-04 ±3.8E-04	1.6E-03 ±6.1E-04	0
D (ps)	t_0 (ps)	X_T	$\tau_{T,ini}$ (ps)	$\tau_{T,rec}$ (ps)	$y_{(10),0}$	$y_{(11),0}$	X_{SF}
0.5	10.7 ±0.9	2.2E-02 ±1.1E-03	16.1 ±2.3	523 ±41	-3.7E-03 ±6.4E-04	-9.7E-03 ±7.7E-04	3.7E-02 ±2.6E-03
1.0	5.4 ±0.7	2.5E-02 ±8.5E-04	12.7 ±1.2	883 ±70	-2.2E-03 ±5.2E-04	-6.5E-03 ±6.3E-04	1.0E-02 ±2.0E-03
1.5	1.2 ±0.7	2.7E-02 ±8.0E-04	10.7 ±1.1	1370 ±142	-4.9E-04 ±5.2E-04	-4.3E-03 ±6.4E-04	2.8E-03 ±2.1E-03
2.0	1.2 ±0.7	2.7E-02 ±8.8E-04	10.2 ±1.1	1208 ±120	-2.8E-04 ±5.5E-04	-4.0E-03 ±6.8E-04	7.0E-07 ±2.3E-03
2.5	-5.1 ±0.7	2.7E-02 ±7.7E-04	9.5 ±1.0	7834 ±4417	3.9E-03 ±5.4E-04	-1.4E-03 ±7.1E-04	9.8E-08 ±2.1E-03

Supplementary Table 3. Summary of fitted parameters for the diffracted beam case. For details of fitting procedure see Supplementary Note 2. Estimated uncertainties correspond to ± 1 standard deviation. $\boldsymbol{\tau_{SF,ini}}$, and $\boldsymbol{\tau_{SF,rec}}$ were set to 24.4 ps and 190.0 ps, respectively, as fixed parameters. These values were the weighted average of the respective parameters in Supplementary Table 1.

Supplementary References

1 Hu, J., Vanacore, G. M., Cepellotti, A., Marzari, N. & Zewail, A. H. Rippling ultrafast dynamics of suspended 2D monolayers, graphene. *Proc. Natl. Acad. Sci.* **113**, E6555-E6561 (2016).

2 R Core Team, R: A language and environment for statistical computing URL https://www.R-project.org/. *R Foundation for Statistical Computing*, Vienna, Austria. (2020).

3 T. V. Elzhov, K. M. Mullen, A. Spiess, B. Bolker, minpack.lm: R interface to the Levenberg-Marquardt nonlinear least-squares algorithm found in MINPACK, Plus Support for Bounds. R package version 1.2-1. https://CRAN.R-project.org/package=minpack.lm (2016).